

Thermal coupling mode in mantle-outer core convection predicted from an ultra-high-resolution numerical simulation of two-layer convection with a large viscosity contrast

Masaki Yoshida*

Department of Physical Sciences, College of Science and Engineering, Ritsumeikan University, 1-1-1, Noji-higashi, Kusatsu, Shiga 525-8577, Japan

ABSTRACT

Previous global mantle seismic tomography analyses have revealed the large-scale horizontal structure of the mantle. On the other hand, the large-scale horizontal structure of the outer core could not be well determined using seismic wave analysis due to its liquid nature. Therefore, at present, numerical simulations are the only method for understanding the horizontal thermal structure of the outer core. Previous numerical studies on two-layer Rayleigh–Bénard convection with an infinite Prandtl number have shown that the coupling mode between the two layers changes from mechanical coupling to a transitional mode to thermal coupling as the viscosity contrast between the two layers increases. This study presents an ultra-high-resolution numerical simulation of two-layer convection with a viscosity contrast of 10^4 . The effective Rayleigh number of convection in the inner low-viscosity layer reached approximately 2×10^{10} . A spatiotemporal analysis of convection confirmed a new thermal coupling mode in the two-layer convection, primarily driven by downwelling plumes. When applied to the coupling between the mantle and outer core of Earth's interior, whose geophysical and geochemical structures are considered nearly hemispherical relative to the axis of rotation, this coupling mode effectively cools Earth's core. Conversely, heat from the Earth's core is slowly released to the Earth's surface via mantle convection.

ARTICLE INFO

History:

Received May 21, 2025

Revised Jun 05, 2025

Accepted Jun 06, 2025

Keywords:

Numerical simulation

Two-layer convection

Mantle convection

Outer core convection

Thermal coupling mode

Citation:

Yoshida, M., 2025. Thermal coupling mode in mantle-outer core convection predicted from an ultra-high-resolution numerical simulation of two-layer convection with a large viscosity contrast. *Habitable Planet* 1(1&2), 145–156.

<https://doi.org/10.63335/j.hp.2025.0012>

© International Association for Gondwana Research & Gondwana Institute for Geology and Environment, Japan

*Email: masakiy@fc.ritsumei.ac.jp

Research Highlights

- An ultra-high-resolution numerical simulation of two-layer convection with a large viscosity contrast of 10^4 was performed in a 2-D spherical geometry.
- Mantle and outer-core convection in the Earth are expected to be coupled under a thermal coupling mode driven by downwelling plumes.
- This coupling mode effectively cools Earth's core, slowly releasing heat from the core to the Earth's surface via mantle convection.

1 Introduction

Our planet consists of multiple layers: atmosphere, seawater, and solid Earth. Most of the Earth's interior ($\sim 99\%$ of the volume of the entire Earth) consists of the mantle and outer core, which are composed of solid rock and molten iron, respectively. The Earth is thought to have evolved over its long history of approximately 4.6 billion years through thermal and mechanical interactions between the mantle and core. The evolution of the solid Earth has impacted climate change and the evolution of life. The combination of the interactions between the solid Earth, atmosphere, and oceans as a single system is called the “Earth System” (e.g., [Condie, 2016](#)).

[Fig. 1](#) shows the coupling modes between the upper high-viscosity layer (HVL) and the lower low-viscosity layer (LVL). When the viscosity contrast between the two layers is equal or sufficiently small, the two layers are mechanically coupled ([Yoshida and Hamano, 2016](#); [Yoshida et al., 2017](#)). In this “mechanical (viscous) coupling mode,” the vertical flows in the two layers move in opposing directions, and the direction of the shear stress that drags the interface between the two layers is identical ([Fig. 1a](#)). As the viscosity contrast between air and water is approximately two orders of magnitude, the atmosphere and ocean must be mechanically coupled. Conversely, in fluid dynamics, the “thermal coupling mode” is suggested as an opposing model to the mechanical coupling mode ([Fig. 1d](#)) ([Xie and Xia, 2013](#); [Sun et al., 2024](#)). In the idealized image of the thermal coupling mode in a two-layer convection without viscosity contrast or with only a small viscosity contrast, the direction of the vertical flow between the two layers is identical ([Ukaji and Sawada, 1970a](#); [Ukaji and Sawada, 1970b](#); [Ukaji and Sawada, 1971](#); [Honda, 1982](#); [Johnson and Narayanan, 1997](#); [Prakash et al., 1997](#)).

Previous global mantle seismic tomography analyses have revealed the large-scale horizontal structure of the mantle (e.g., [Ritsema et al., 2011](#); [French and Romanowicz, 2014](#); [Zhao, 2015](#); [Lu et al., 2019](#)). However, the large-scale horizontal structure of the outer core cannot be determined from seismic wave analysis because S waves do not pass through the outer core composed of fluid iron, and only a limited number of P waves are incident on the outer

core. Therefore, numerical simulations are the only viable method for furthering our understanding of the large-scale structure of the outer core.

Previous numerical studies of two-layer Rayleigh–Bénard convection with an infinite Prandtl number have indicated that the coupling mode between the two layers changes from a mechanical coupling mode to a “transitional mode,” as the viscosity contrast between the two layers increases ([Yoshida and Hamano, 2016](#); [Yoshida et al., 2017](#)) ([Fig. 1b](#)). In the transitional mode, the flow pattern in the LVL periodically switches between two phases (i.e., the mechanical and thermal coupling phases), separated by a stagnation period. When the viscosity contrast is 10^2 – 10^3 , the temporal frequency required for switching is several million years ([Yoshida et al., 2017](#)).

The thermal coupling mode in two-layer Rayleigh–Bénard convection with a large viscosity contrast has not been investigated in previous studies. This is because (1) numerical simulations are the only viable method for studying thermal convection with an infinite Prandtl number and (2) the most advanced supercomputers are required to numerically resolve the thin thermal boundary layer of ultra-high Rayleigh number convection. This study performed an ultrahigh-resolution numerical simulation of two-layer Rayleigh–Bénard convection with a viscosity contrast of 10^4 .

2 Numerical model

The computational domain was confined in a two-dimensional (2-D) spherical-shell geometry with a radius of $r_{\text{top}} = 6,371$ km and thickness of $b = 5,149.5$ km along spherical polar coordinates (r, θ) , consisting of an outer HVL and inner LVL ([Fig. 2](#)). The thicknesses of the HVL and LVL were fixed at 2,891 and 2,258.5 km, respectively, which correspond to the thicknesses of the mantle and outer core of the Earth. The mechanical and thermal boundary conditions at the top and bottom boundaries were impermeable, shear-stress-free, and isothermal. The layer was heated at the bottom-surface boundary and cooled to the top-surface boundary.

The conservation equations for the mass, momentum, and energy of thermal convection with an infinite Prandtl

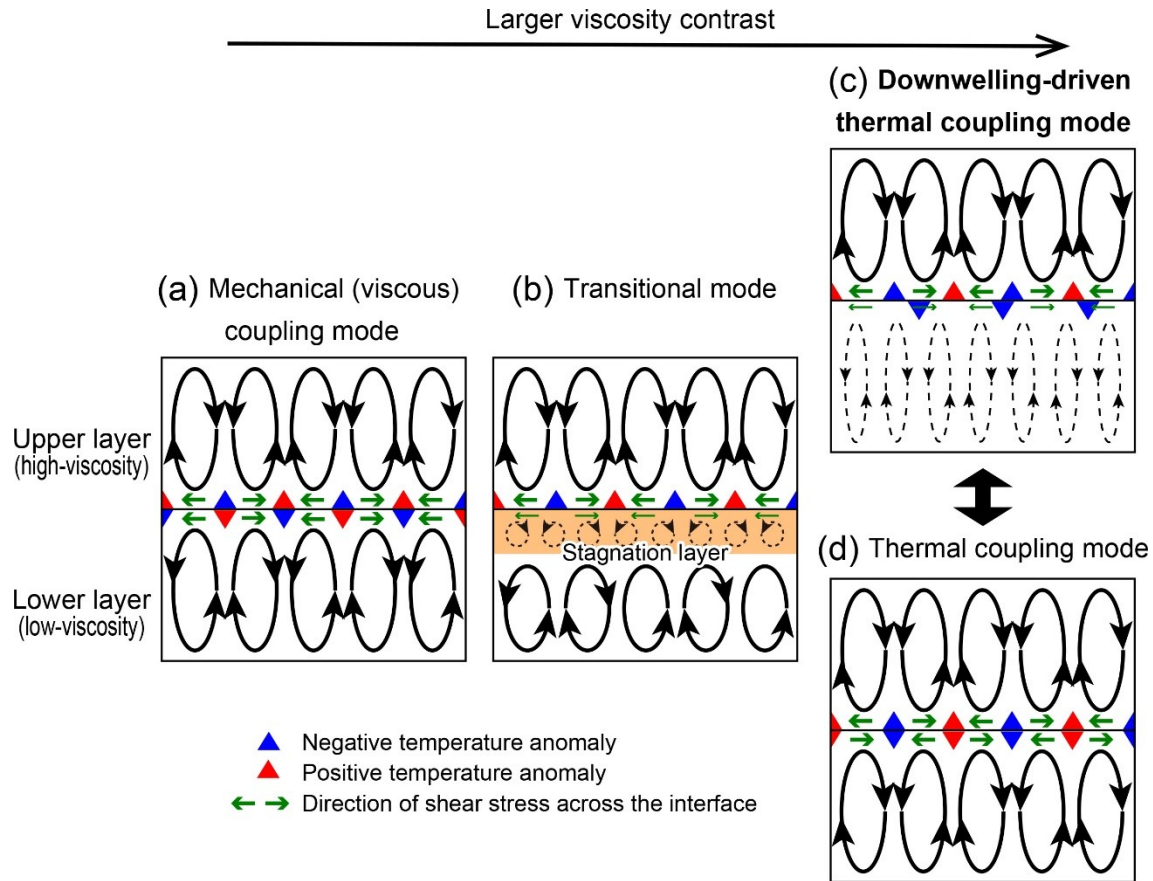


Fig. 1. Cartoon of the different coupling modes for two-layer Rayleigh–Bénard convection with a viscosity contrast. (a) Mechanical (viscous) coupling mode, (b) transitional mode, (c) “downwelling-driven thermal coupling mode” proposed in the present study, and (d) idealized thermal coupling mode. The solid and dashed black arrows indicate the flow direction, and the green arrows indicate the direction of shear stress across the interface between the two layers. The blue and red triangles indicate the negative and positive temperature anomalies, respectively.

number under the Boussinesq approximation have the following dimensionless forms (e.g., Schubert et al., 2001; Yoshida, 2017):

$$\nabla \cdot \mathbf{v} = 0, \quad (1)$$

$$0 = -\nabla p + \nabla \cdot \boldsymbol{\sigma} + \alpha_0 \left[1 + \gamma \xi \frac{Rb}{Ra} f(r) \right] TRa \xi^{-3} \mathbf{e}_r, \quad (2)$$

$$\frac{\partial T}{\partial t} + \mathbf{v} \cdot \nabla T = \nabla^2 T, \quad (3)$$

where \mathbf{v} is the velocity, p is the dynamic pressure, $\boldsymbol{\sigma}$ is the deviatoric stress, η is the viscosity, t is the time, T is the temperature, α_0 is the coefficient of thermal expansion of the HVL, and \mathbf{e}_r is the radial component of the unit vector (positive for upward direction). The constitutive equation is given by

$$\boldsymbol{\sigma} = \eta [(\nabla \mathbf{v}) + (\nabla \mathbf{v})^T] \quad (4)$$

where superscript T indicates the tensor transpose. The adiabatic and viscous dissipation heating were not considered in the energy conservation equation (Eq. (3)).

A key feature of the proposed numerical model is that the two layers are continuously thermally and mechanically coupled. Following a previous study, a function of the Gaussian-type phase distribution, $f(r)$, with a peak of the effective thermal expansion coefficient at the interface of the two layers was introduced in the buoyancy term of Eq. (2), to realize thermally and mechanically continuous two-layer convection (Yoshida and Hamano, 2016; Yoshida et al., 2017). Function $f(r)$ is given by

$$f(r) = \frac{1}{2\omega} \exp \left[- \left(\frac{r - r_{\text{intf}}}{\omega} \right)^2 \right], \quad (5)$$

where r_{intf} is the radius of the interface between the two layers, 3,480 km; and ω is the half-width of the transition boundary. For the simplicity of the numerical model, the depth of the boundary between the HVL and LVL was fixed in space and time and independent of physicochemical circumstances.

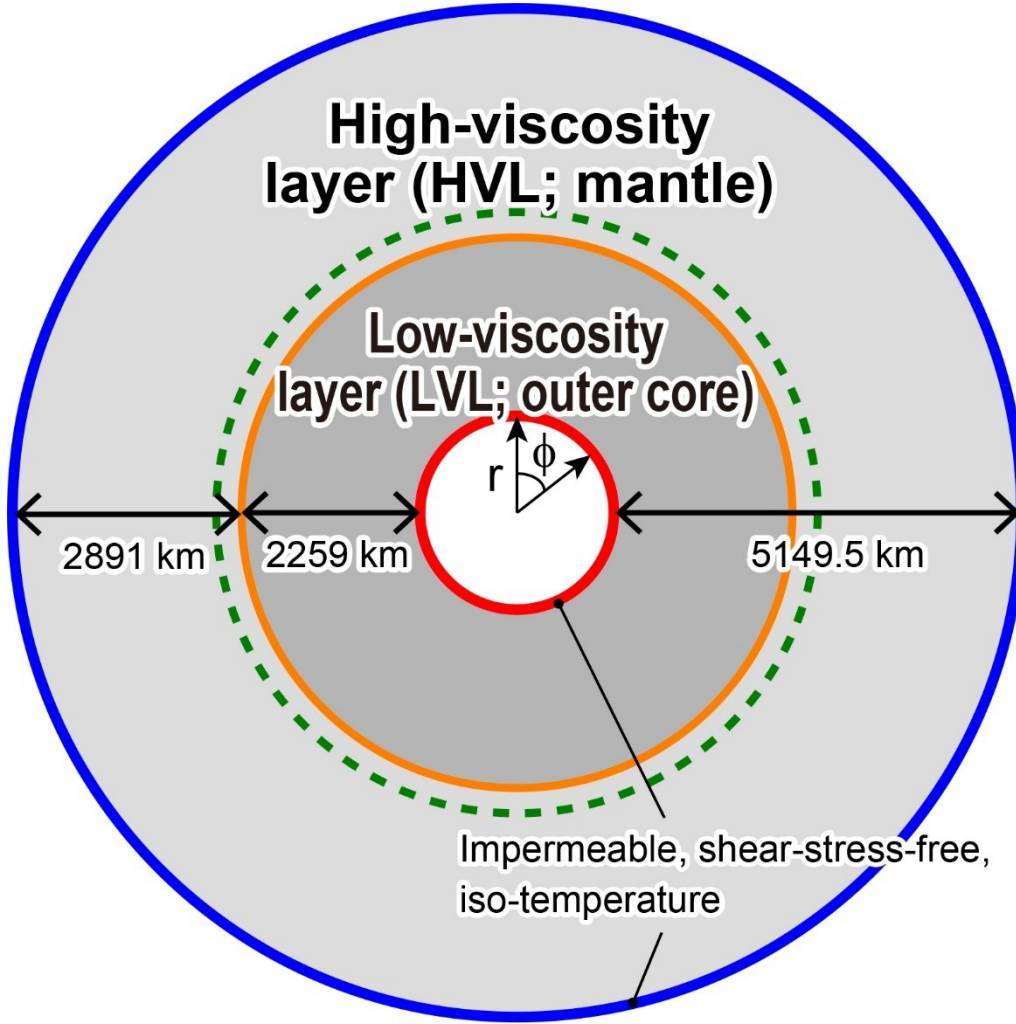


Fig. 2. Numerical model for two-layer Rayleigh–Bénard convection with a highly viscous layer (HVL) in the outer shell and low-viscosity layer (LVL) in the inner shell for a two-dimensional (2-D) spherical-shell geometry. The orange circle indicates the interface between the HVL and LVL. The radial computational grids in the lower part below the green dashed circle are 15 times finer than those in the upper part.

The dimensionless parameters in Eq. (2) are the thermal Rayleigh number (Ra), boundary layer number (Rb), layering parameter (γ), and ratio of the thickness of the convection layer to the radius at the top surface boundary (ξ):

$$\begin{aligned} Ra &\equiv \frac{\rho_{H0}\alpha_0\Delta T g_0 b^3}{\kappa_0\eta_{H0}}, & Rb &\equiv \frac{\Delta\rho_L g_0 b^3}{\kappa_0\eta_{H0}}, \\ \gamma &\equiv \frac{\Delta T \Xi}{\rho_{H0} g_0 b}, & \xi &\equiv \frac{b}{r_{\text{top}}}, \end{aligned} \quad (6)$$

where ρ_{H0} is the density of the HVL, $\Delta\rho_L$ is the density difference between the two layers, ΔT is the temperature drop across the convection layer, g_0 is the gravitational acceleration, κ_0 is the thermal diffusivity, η_{H0} is the viscosity of the HVL, and Ξ is the degree of layering (subscript “0”

indicates the reference value in the HVL). The values of the quantities and dimensionless parameters are listed in Tables S1 and S2, respectively, in the Supplementary Material.

The viscosity is spatiotemporally constant in each layer. The reference viscosity of the HVL was fixed at $\eta_{H0} = 10^{22}$ Pa s, which is the typical viscosity of the Earth’s lower mantle (e.g., Lau et al., 2016; Lambeck et al., 2017; Argus et al., 2021). In contrast, the viscosity of the LVL, η_L , was taken as a free parameter in previous studies and set to 10^{18} Pa s in this study. Thus, in this study, the viscosity contrast between the HVL and LVL, $\Delta\eta_L = \eta_{H0}/\eta_L$, was set to 10^4 , in contrast to previous studies in which $\Delta\eta_L$ reached approximately 10^3 (Yoshida and Hamano, 2016; Yoshida et al., 2017). The viscosity contrast of 10^4 is a higher limit value considering the current computational power, even

when performing parallel computation using 1,024 cores in the Earth Simulator supercomputer at the Japan Agency for Marine-Earth Science and Technology.

The thermal convection was computed using a staggered grid and finite-volume-based code ConvRS (Yoshida, 2010). The Semi-implicit Method for Pressure-Linked Equations Revised (SIMPLER) algorithm was used to compute the velocity and pressure fields on a staggered grid (Versteeg and Malalasekera, 2007; Ferziger et al., 2020). A multicolor relaxation scheme was used to solve the coupled equations in Eqs. (1) and (2) using the SIMPLER algorithm.

The numbers of the finite volumes were 4,096 and 4,096 in the radial and longitudinal directions, respectively. The grid intervals for the longitudinal direction were ~ 9.7 and ~ 1.9 km at the top and bottom surface boundaries. The grid interval in the lower part of the spherical shell was 15 times finer than that in the upper part; thus, the radial grid intervals in the upper and lower parts of the spherical shell were ~ 10.1 and ~ 0.7 km. In the preliminary run, the thicknesses of the thermal boundary layers at the top and bottom surfaces of the LVL were approximately 35 and 7 km, respectively, when the viscosity contrast between the HVL and LVL was set to 10^4 . Therefore, the grid numbers across the thermal boundary layers are ~ 50 ($= \sim 35/0.7$) and ~ 10 ($= \sim 7/0.7$), respectively, which are significantly larger than the minimum required number of grid intervals (i.e., at least three grid intervals), guaranteeing the accuracy of the numerical solution of the Rayleigh–Bénard convection (McKenzie and Parker, 1967; Moore and Weiss, 1973).

The initial condition of the thermal field used a previous solution of convection with $\Delta\eta_L = 10^3$ (Yoshida et al., 2017). After the temperature and velocity fields reached a statistically steady state, the simulation was performed for ~ 1000 million years (Myr), which is a sufficiently long timescale comparable to Earth’s history.

3 Results

Fig. 3 shows snapshots of the temperature and velocity fields obtained from the simulations. The convection speed of the HVL is of the order of 1 cm yr^{-1} , which is comparable to the convection speed of the mantle, whereas that of the LVL is of the order of 100 cm yr^{-1} . The convection pattern of the HVL has remained stable for approximately 100 million years, whereas that of the LVL has exhibited a strong time dependence (see Movie 1 in Appendix). The convection pattern of the HVL becomes more stable as the viscosity contrast between the HVL and LVL increases (Yoshida and Hamano, 2016; Yoshida, 2023a). This is because when the viscosity contrast increases, the coupling model between the two layers switches from a purely mechanical coupling mode to a different coupling mode.

The previous numerical model with $\Delta\eta_L$ of up to 10^3 demonstrated that the temporally averaged temperatures in the HVL and LVL increased with increasing $\Delta\eta_L$. Fig. 4 shows that this trend was confirmed even when $\Delta\eta_L = 10^4$ (red curve in Fig. 4a). The effective Rayleigh number in each layer is defined as follows:

$$Ra_{\text{eff}} \equiv \frac{\rho\alpha_0 \langle \Delta T \rangle g_0 b^3}{\kappa_0 \eta_{H0}}, \quad (7)$$

where $\langle \Delta T \rangle$ denotes the temporally averaged temperature difference across the layers. Because the average temperature of the interface between the two layers is ~ 1800 °C, Ra_{eff} of the HVL was estimated as $\sim 4.2 \times 10^6$, and Ra_{eff} of the LVL was estimated as $\sim 1.8 \times 10^{10}$, which is a sufficiently large Rayleigh number for realizing chaotic convective flow (Fig. 3b).

In the LVL, the thermal boundary layer of the top surface (“P” in Fig. 4b) is thicker than that of the bottom surface (“Q” in Fig. 4c). The downwelling instability that developed in the thick thermal boundary layer (Fig. 3b) was caused by a large heat flux at the interface between the two layers, which was due to the downwelling plumes of the HVL. Concurrently, the upwelling plume originating from the bottom thermal boundary layer of the LVL contributes to the emergence of downwelling instability. Previous numerical simulations of thermal convection with an infinite Prandtl number and Rayleigh number of 1×10^{10} demonstrated that upwelling plumes are extremely weak and cannot reach the top surface boundary layer (Vecsey, 2003; Vecsey et al., 2003). In contrast, in the LVL of the present simulation, the upwelling plumes originating at the bottom surface boundary were sufficiently strong to reach the top surface boundary layer (Fig. 3b) owing to the return flow of the strong downwelling plumes.

Fig. 5a and b demonstrate a spatiotemporal analysis of the temperature anomaly (δT) field (i.e., temperature deviation from average at each radius) across the interface between the two layers. The patterns of radial and longitudinal velocities correspond to that of δT (Fig. 6a and b). At the mid-depth of HVL (i.e., a radius of 4,925.5 km), the distributions of negative and positive δT exhibit a striped pattern, indicating that the longitudinal locations of the downwelling and upwelling plumes in the HVL are practically stationary against the long-elapsed time (Fig. 5a). Conversely, in the LVL, the patterns of negative and positive δT are chaotic, indicating that the behavior of downwelling and upwelling plumes is spatiotemporally vigorous (Fig. 5b). The most striking feature of the convection in the LVL is that the low temperature-anomaly region (wide blue band marked by “L” in Fig. 5b) dominates the time-space rather than the high temperature-anomaly region (narrow red band marked by “H” in Fig. 5b). This indicates that convection in the LVL was primarily dominated by the downwelling flow. In this study, this coupling mode is called

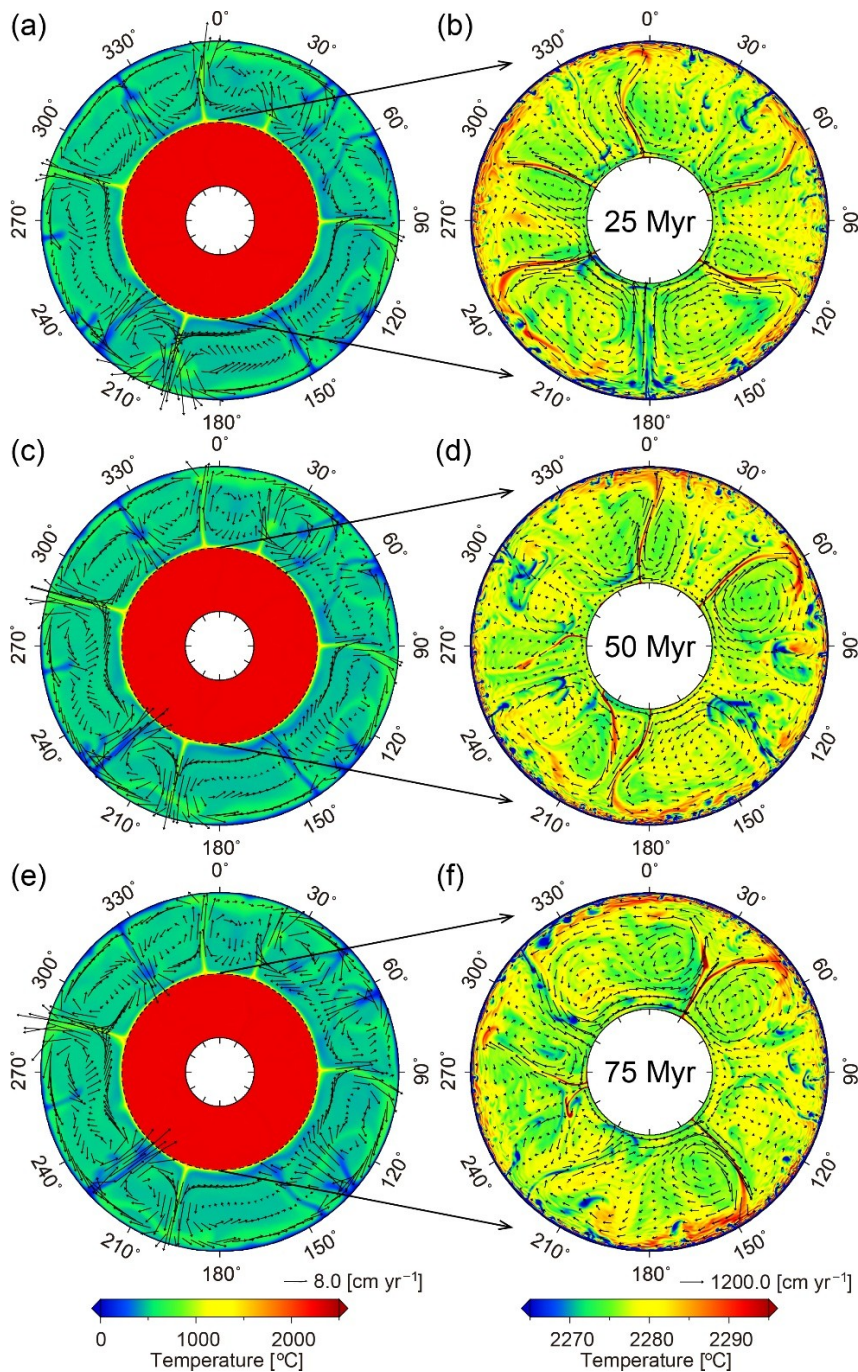


Fig. 3. Snapshots of temperature and velocity fields in the HVL and LVL (a, c, and e), with close-up views focusing on the interior of the LVL (b, d, and f). The viscosity contrast between the HVL and LVL is $\Delta\eta_L = 10^4$. The elapsed times are (a and b) ~ 25 Myr, (c and d) ~ 50 Myr, and (e and f) ~ 75 Myr from the start of the simulation. See also Movie 1 in Appendix.

as “downwelling-driven thermal coupling mode” (Fig. 1c), in contrast to the well-known “thermal coupling mode” observed in a two-layer thermal convection with a low Prandtl number, in which the upwellings and downwellings are synchronized between the two layers (Fig. 1c).

The shear stress across the interface is defined by

$$\tau_{\phi r} = \eta \left(\frac{1}{r} \frac{\partial v_r}{\partial \phi} + \frac{\partial v_\phi}{\partial r} - \frac{v_\phi}{r} \right), \quad (8)$$

where v_r and v_ϕ are the radial and longitudinal velocities.

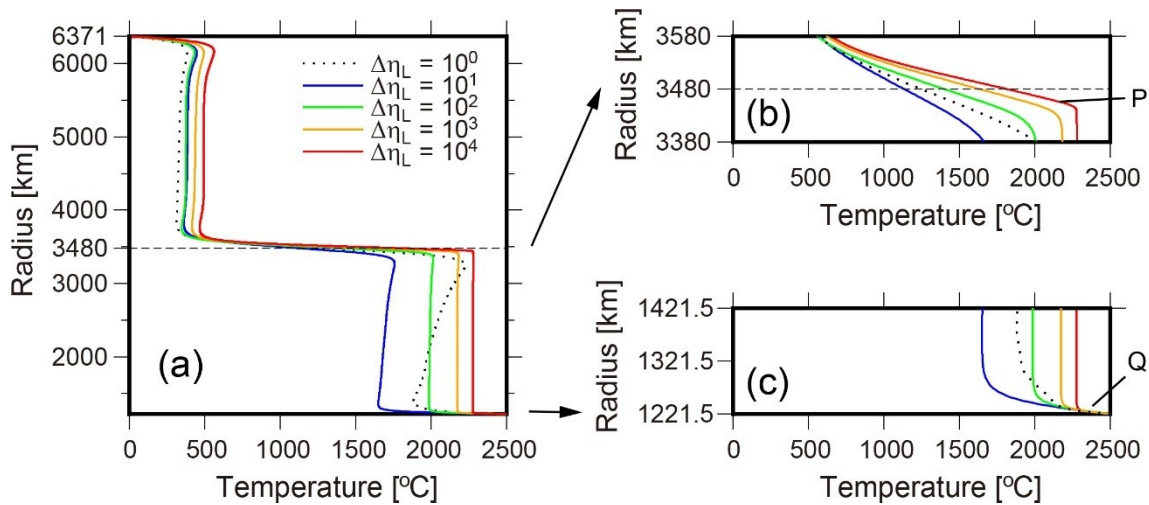


Fig. 4. (a) Radial profiles of the temporally averaged temperatures at each radius for the models with a viscosity contrast of $\Delta\eta_L = 1$ (i.e., no viscosity contrast between the LVL and HVL, dotted black), 10^1 (blue), 10^2 (green), 10^3 (orange), and 10^4 (red). (b and c) Close-up view focusing on the profiles near the interface between the two layers at a radius of 3,480 km (b) and the bottom surface boundary at a radius of 1,221.5 km (c).

In the idealized thermal coupling mode, the direction of the shear stress across the interface should be the opposite (Fig. 1c). In contrast, in the downwelling-driven thermal coupling mode, the directions of shear stress across the interface are identical, indicating that negative (positive) $\tau_{\phi r}$ just above the interface corresponds to the negative (positive) $\tau_{\phi r}$ just below the interface (Fig. 5c and d). The corresponding normal stresses in the radial and longitudinal directions across the interface show that the upwelling plumes exert tension on the interface and the downwelling plumes exert compression on the interface (Fig. 6c and d). This mechanical interaction between the two layers also provides evidence that the two-layer convection shown in Fig. 3 consists of a new thermal-coupling mode that has not been presented in previous studies.

4 Discussion

4.1 Implications for the top-down dynamics of the Earth

On Earth, the lower mantle is a solid silicate layer with perovskite and post-perovskite compositions, whereas the outer core is a fluid iron-nickel alloy. Therefore, although the lower mantle is slightly cooler, it is still lighter than the underlying liquid core, preventing mass transfer from the mantle to the core. Nevertheless, heat transfer from the mantle to the core may be possible via a thermal boundary layer between the two (i.e., core-mantle boundary; CMB). In the downwelling-driven thermal coupling mode, in which the upwelling flow is not directly linked between the two layers (Fig. 1c), heat is transported relatively slowly from the LVL to the HVL compared to the idealized thermal coupling mode (Fig. 1d). This is consistent the extremely slow cool-

ing of the Earth ($\sim 80^\circ\text{C}$ over 1 billion years) (e.g., Herzberg et al., 2010).

Based on recent geochemical and geophysical observations of the Earth, lateral variations in water distribution, seismic velocity, and electrical conductivity of the mantle show a hemispherical structure (Iwamori and Nakamura, 2015; Iwamori et al., 2022) (Fig. 7). A top-down link from the supercontinents through the mantle and outer core to the inner core has been proposed; namely, surface tectonics (i.e., cold-plate subduction) control the formation of large-scale structures throughout the entire solid Earth. The convection pattern and heat transfer between the two layers obtained in the present simulation imply that convection in the highly viscous mantle controls convection in the extremely low-viscosity outer core in a top-down manner. Such thermal and mechanical interactions between the mantle and the outer core can be explained by the downwelling-driven thermal coupling mode proposed in this study. This coupling mode effectively cools the core and releases heat from the deep Earth to the surface.

The behavior of subducting plates is crucial to the top-down dynamics hypothesis. Several studies have suggested that the subducting plates are not driven by negative buoyancy (i.e., slab pull) (e.g., Cruciani et al., 2005; Faccincani et al., 2021). Faccincani et al. (2021) demonstrated that the density of the oceanic lithosphere is smaller than the underlying asthenosphere through a theoretical mineral physics analysis. In truth, understanding the main driving force behind plate subduction remains one of the major challenges in modern geophysics. Recently, using an instantaneous global mantle flow calculation, Yoshida (2023b) demonstrated that buoyancy-induced

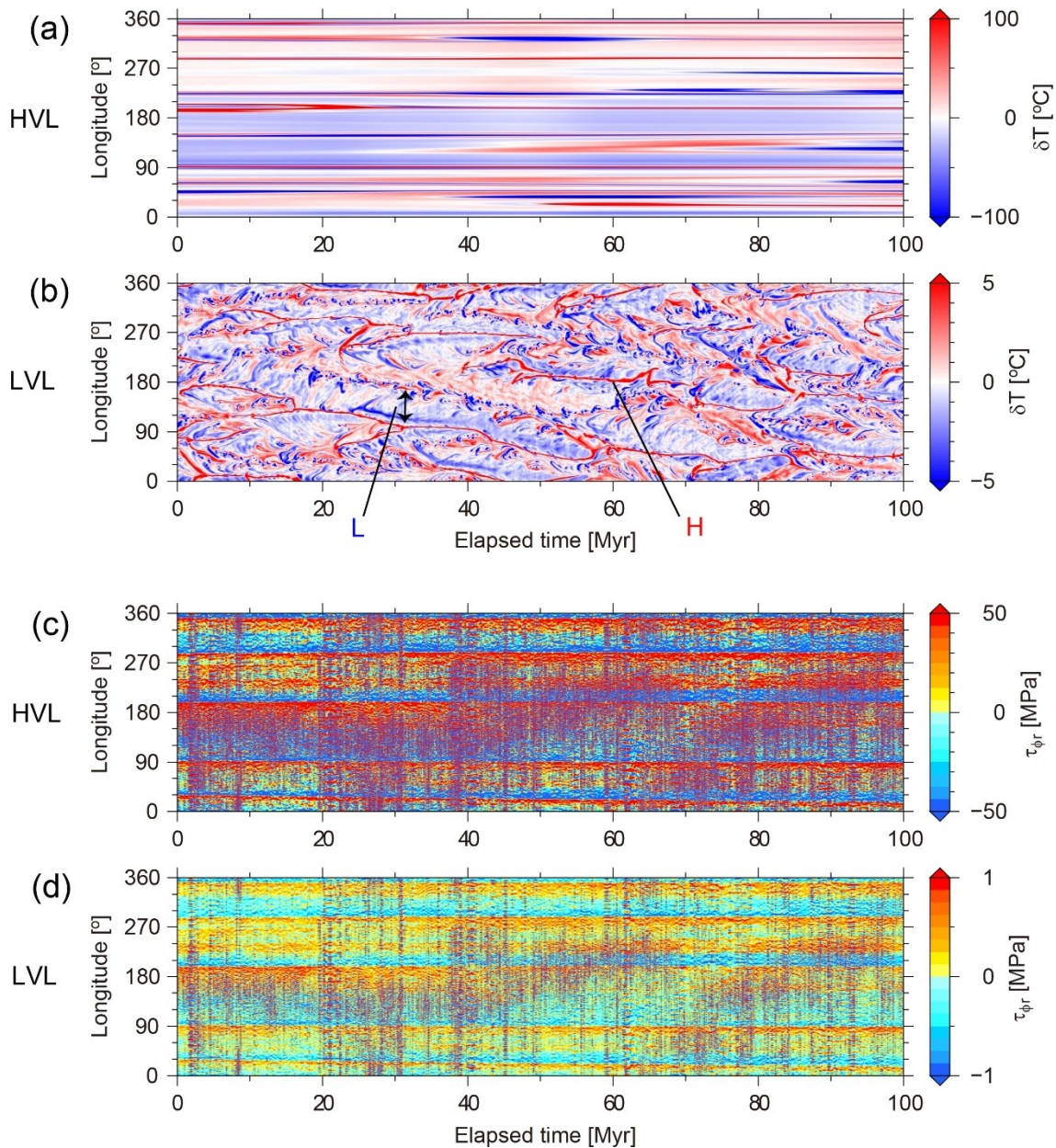


Fig. 5. (a and b) Longitudinal and temporal variations of the temperature anomaly (δT) at mid-depth of the HVL (i.e., radius of 4925.5 km; a) and at mid-depth of LVL (i.e., radius of 2350.8 km; b). “L” and “H” indicate the low and high temperature-anomaly areas, respectively. (c and d) Longitudinal and temporal variations of the shear stress ($\tau_{\phi r}$) just above (c) and below the interface between the two layers (d). The shear stress ($\tau_{\phi r}$) is positive at $\phi = 360^\circ$.

asthenospheric flow in the shallow upper mantle is essential for reproducing the observed plate motion of the Pacific Plate, indicating that the primal driving force of the plate motion is mantle drag. In any case, the large amount of subducted plate accumulated at the CMB may affect the temperature structure of the uppermost part of the outer core.

For simplicity, the present model is based on the Boussinesq approximation; thus, adiabatic heating is not

considered in the HVL. However, the lower mantle is considered to have subadiabatic conditions, meaning that the potential temperature is too low to stimulate mantle convection (e.g., Birch, 1951; Jeanloz and Morris, 1987). Anderson (2002) suggested that irreversible mantle stratification was caused by convection in the mantle, which conveyed higher-density elements (e.g., Fe) into the lower mantle, thereby enhancing mantle stratification. However, even when adiabatic temperature gradients are incorporated

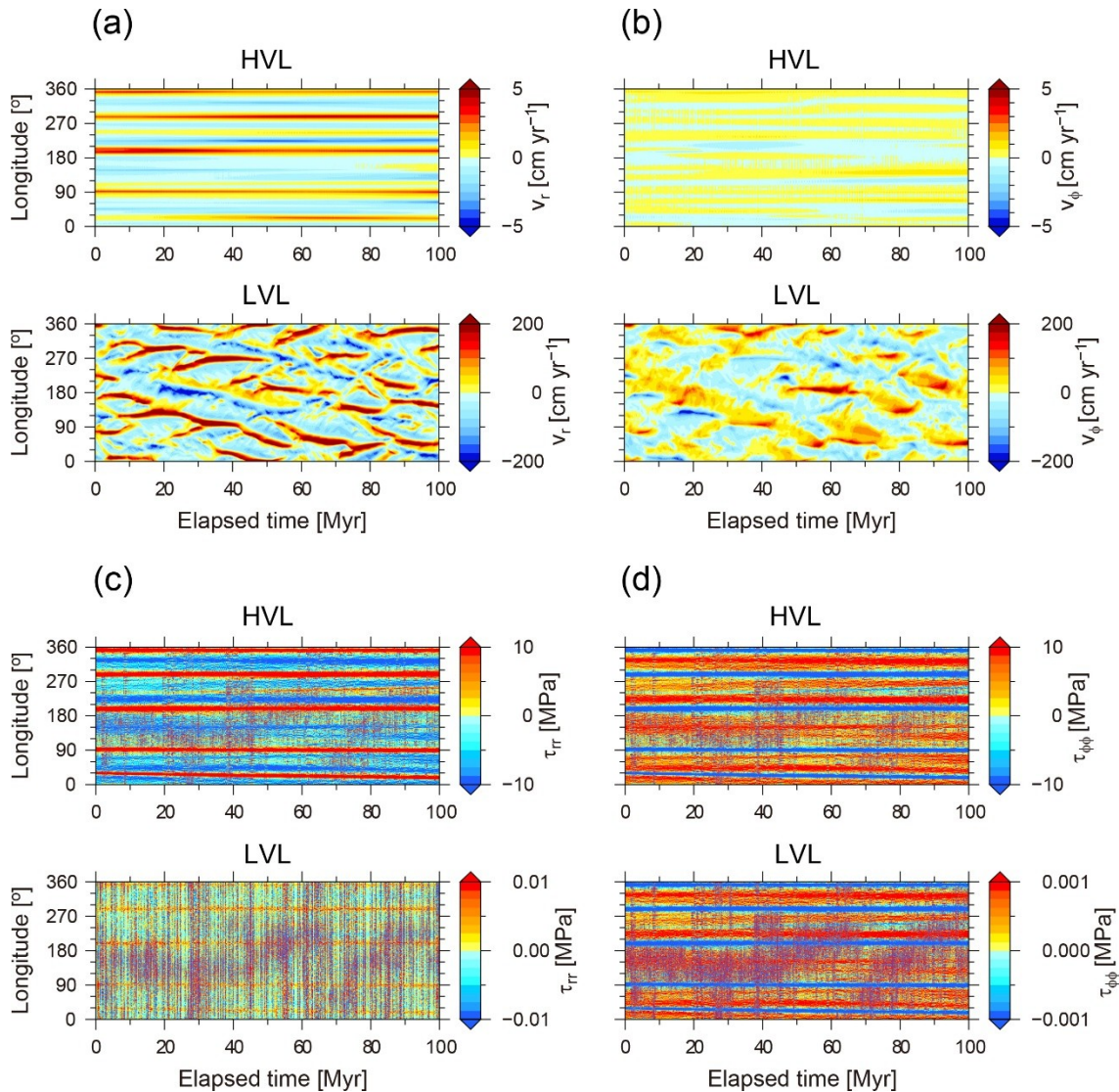


Fig. 6. (a) Longitudinal and temporal variations of the vertical velocity (v_r) at mid-depth of the HVL (i.e., radius of 4925.5 km; upper panel) and LVL (i.e., radius of 2350.8 km; lower panel). The vertical velocity (v_r) is positive upward. (b) Longitudinal and temporal variations of the longitudinal velocity (v_ϕ) at mid-depth of the HVL (i.e., radius of 4925.5 km, upper panel) and at LVL (i.e., radius of 2350.8 km, lower panel). The longitudinal velocity (v_ϕ) is positive at $\phi = 360^\circ$. (c) Longitudinal and temporal variations of the normal stress in the radial direction (τ_{rr}) above (upper panel) and below (lower panel) the interface between the two layers. (d) Longitudinal and temporal variations of the normal stress in the longitudinal direction ($\tau_{\phi\phi}$) above (upper panel) and below (lower panel) the interface. The normal stresses in each direction are given by $\tau_{rr} = 2\eta(\partial v_r/\partial r)$ and $\tau_{\phi\phi} = 2\eta(\partial v_\phi/r\partial\phi + v_r/r)$, where v_r and v_ϕ are the radial and longitudinal velocities and η is the viscosity. Negative and positive values indicate the compressive and tensional stresses, respectively.

into numerical simulations of mantle convection, the subducting plates still reach the CMB (e.g., Yoshida, 2008b). Indeed, seismic tomography models consistently detect high-velocity seismic anomalies above the CMB, that represent the accumulation of subducted plates (e.g., Ritsema et al., 2011; French and Romanowicz, 2014; Zhao, 2015; Lu et al., 2019).

4.2 Future directions for the whole solid-Earth numerical simulation

Because the geometry of the actual Earth is spherical, the present 2-D model must be updated to a 3-D model as supercomputers become more advanced in the future. Recently, Demou et al. (2024) performed direct numerical

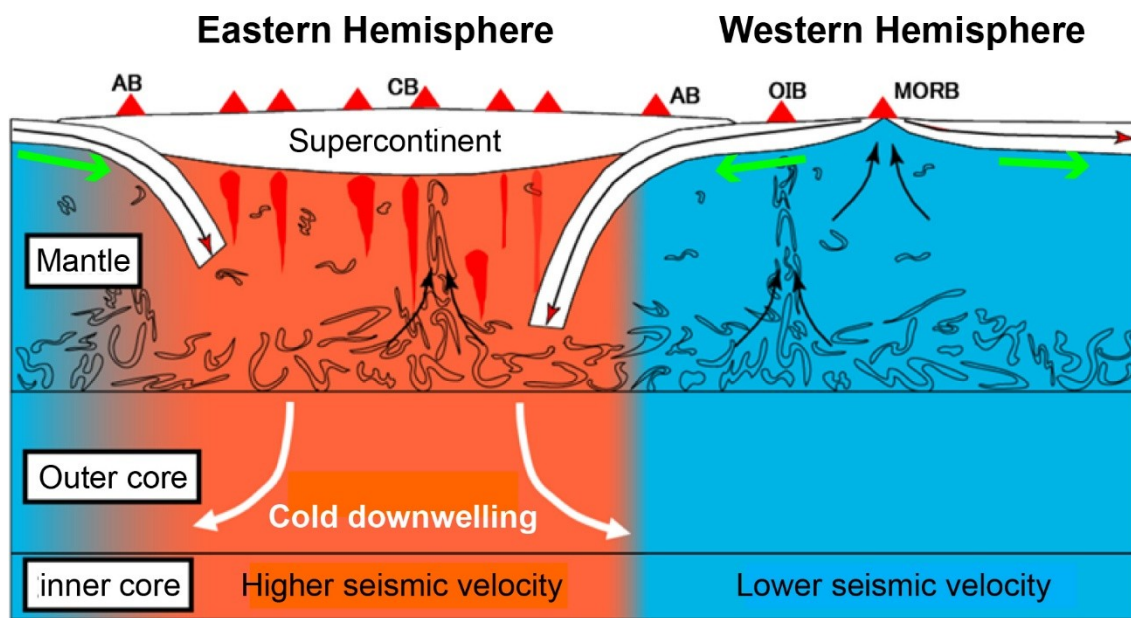


Fig. 7. Schematic illustration of “top-down hemispherical dynamics” of the Earth’s interior from geochemical and geophysical observations modified from previous publications (Iwamori and Nakamura, 2015; Iwamori et al., 2022). The many streaks in the mantle indicate the melt component that accumulates near the boundary between the mantle and outer core. In the Eastern Hemisphere (orange region), the hydrophile component is enriched in the mantle and the seismic velocity in the inner core is relatively high, whereas in the Western Hemisphere (cyan region), the hydrophile component is depleted in the mantle and the seismic velocity in the inner core is relatively low. The existence of large-scale cold downwelling in the outer core of the Eastern Hemisphere (white solid arrows) is proposed in this study. The green arrows under the plates indicate mantle drag.

simulations to study two-layer Rayleigh–Bénard convection with a low Prandtl number and $10^6 \leq Ra \leq 10^8$ in 3-D Cartesian space. In contrast, the present numerical model is limited to a 2-D spherical shell geometry owing to the constraints of current computational power. However, because columnar cells parallel to the axis of rotation dominate the extremely low-viscosity outer core of the real Earth (e.g., Busse, 1970; Kono and Roberts, 2002), the present 2-D spherical shell model is reasonable and approximates convection along a cross-section of the equator. Furthermore, aiming for a “Whole Solid-Earth Numerical Simulation” (Yoshida, 2023a), future 3-D models will need to consider the growth of the inner core.

The major limitation of the present numerical model is that the studied convection regime is not directly applicable to the fluid core. In the core, the largest dynamic term is the Coriolis force, and the main force balance is magnetostrophic (i.e., the Coriolis, pressure, buoyancy, and Lorentz forces). The inertial accelerations were orders of magnitude larger than those of the viscous forces. Even if we focus on pure thermal convection (neglecting the Lorentz force), the first-order dynamics of convection in the fluid core must include the Coriolis force and acceleration terms. These effects must be considered in future two-layer convection models with larger viscosity contrasts

between the HVL with an infinite Prandtl number and the LVL with a finite Prandtl number. In such cases, further advances in supercomputer capabilities are required to develop higher-resolution models.

As stated in Section 2, in the present model, the depth of the boundary between the HVL and LVL is fixed in space and time. In the real Earth, in contrast with earlier seismological results revealing that large-scale topographic amplitudes exceeds $\pm\sim 4$ km (e.g., Morelli and Dziewonski, 1987), more recent studies have implied smaller peak amplitudes of $\pm\sim 1.5$ km (e.g., Koper et al., 2003; Sze and van der Hilst, 2003; Tanaka, 2010). A numerical study using the instantaneous mantle flow model suggested that, to account for the small CMB topography inferred from these seismological results, lateral viscosity variations in the mantle, compositionally dense piles in the deep mantle, and a low-viscosity D” layer are required for the numerical models (Yoshida, 2008a). Using a 2-D numerical simulation of mantle convection, Heyn et al. (2020) predicted a short-wavelength topographic depression with a width of ~ 100 km surrounding the thermo-chemical pile, named Large Low Shear Velocity Provinces (LLSVPs). They suggested that the depth of this depression depends on the viscosity contrast between the surrounding mantle and these piles. If such small-scale CMB topography be-

comes seismologically observable in the future, the validity of the numerical simulation models used in this and previous studies can be verified.

5 Conclusions

In this study, to investigate the coupling mode in mantle and outer-core convection of the Earth, an ultra-high-resolution numerical simulation of two-layer convection with a viscosity contrast of 10^4 was performed using 1,024 cores in a supercomputer. The concluding remarks are as follows.

1. The effective Rayleigh number of convection in the inner low-viscosity layer reached approximately 2×10^{10} , which is the larger than those used in previous numerical simulations of thermal convection with an infinite Prandtl number.
2. The spatiotemporal analysis of convection confirmed a new thermal coupling mode in two-layer convection, primarily driven by downwelling plumes, called “downwelling-driven thermal coupling mode” in the present study. This coupling mode is different from the standard “thermal coupling mode” in two-layer convection with the constant viscosity.
3. When applied to the coupling between the mantle and outer core of the Earth’s interior, whose geophysical and geochemical structures are considered nearly hemispherical relative to the axis of rotation, this coupling mode effectively cools the core. Conversely, heat from the Earth’s core is being slowly released to the Earth’s surface via mantle convection.

Appendix

Movie 1 can be found at <https://doi.org/10.5281/zenodo.14226711>. This movie shows the temperature and velocity fields in the highly viscous layer (HVL) and low-viscosity layer (LVL) (left panels) with close-up views focusing on the interior of the LVL (right panels). The viscosity contrast between the HVL and LVL was $\Delta\eta_L = 10^4$.

Acknowledgements

I would like to thank two anonymous reviewers for their careful review and thoughtful comments, which have helped me to largely improve the manuscript. Several figures were produced using Generic Mapping Tools (Wessel et al., 2019). Simulations were performed using the Earth Simulator (ES4) at the Japan Agency for Marine-Earth Science and Technology.

CRedit authorship contribution statement

Masaki Yoshida: Writing—Review & Editing, Writing—Original draft, Visualization, Validation, Supervision, Soft-

ware, Resources, Project administration, Methodology, Investigation, Funding acquisition, Formal analysis, Data curation, and Conceptualization.

Declaration of competing interest

The author declares that he has no known competing financial interests or personal relationships that could have influenced the work reported in this paper.

Supplementary material

Supplementary information for this article can be found online at <https://doi.org/10.63335/jp.hp.2025.0012>.

References

- Anderson, D.L., 2002. The case for irreversible chemical stratification of the mantle. *Int. Geol. Rev.* 44(2), 97–116. doi:10.2747/0020-6814.44.2.97.
- Argus, D.F., Peltier, W.R., Blewitt, G., Kreemer, C., 2021. The viscosity of the top third of the lower mantle estimated using GPS, GRACE, and relative sea level measurements of glacial isostatic adjustment. *J. Geophys. Res: Solid Earth* 126(5), e2020JB021537. doi:10.1029/2020JB021537.
- Birch, F., 1951. Elasticity and constitution of the Earth’s interior. *Trans. N. Y. Acad. Sci.* 14, 72–76.
- Busse, F.H., 1970. Thermal instabilities in rapidly rotating systems. *J. Fluid Mech.* 44(3), 441–460. doi:10.1017/S0022112070001921.
- Condie, K.C., 2016. *Earth as an Evolving Planetary System*. Academic Press, Amsterdam, Netherlands. doi:10.1016/C2015-0-00179-4.
- Cruciani, C., Carminati, E., Doglioni, C., 2005. Slab dip vs. lithosphere age: no direct function. *Earth Planet. Sci. Lett.* 238(3), 298–310. doi:10.1016/j.epsl.2005.07.025.
- Demou, A.D., Scapin, N., Ciralessi-Esposito, M., Costa, P., Spiga, F., Brandt, L., 2024. Effects of Rayleigh and Weber numbers on two-layer turbulent Rayleigh–Bénard convection. *J. Fluid Mech.* 996, A23. doi:10.1017/jfm.2024.805.
- Faccincani, L., Faccini, B., Casetta, F., Mazzucchelli, M., Nestola, F., Coltorti, M., 2021. EoS of mantle minerals coupled with composition and thermal state of the lithosphere: inferring the density structure of peridotitic systems. *Lithos* 404–405, 106483. doi:10.1016/j.lithos.2021.106483.
- Ferziger, J.H., Perić, M., Street, R.L., 2020. *Computational Methods for Fluid Dynamics*. 4th ed., Springer, Switzerland, p. 596. doi:10.1007/978-3-319-99693-6.
- French, S.W., Romanowicz, B.A., 2014. Whole-mantle radially anisotropic shear velocity structure from spectral-element waveform tomography. *Geophys. J. Int.* 199(3), 1303–1327. doi:10.1093/gji/ggu334.
- Herzberg, C., Condie, K., Korenaga, J., 2010. Thermal history of the Earth and its petrological expression. *Earth Planet. Sci. Lett.* 292(1–2), 79–88. doi:10.1016/j.epsl.2010.01.022.
- Heyn, B.H., Conrad, C.P., Trønnes, R.G., 2020. Core-mantle boundary topography and its relation to the viscosity structure of the lowermost mantle. *Earth Planet. Sci. Lett.* 543, 116358. doi:10.1016/j.epsl.2020.116358.
- Honda, S., 1982. Numerical analysis of layered convection: marginal stability and finite amplitude analyses. *Bull. Earthq. Res. Inst.* 57, 273–302. doi:10.15083/0000032992.
- Iwamori, H., Nakamura, H., 2015. Isotopic heterogeneity of oceanic, arc and continental basalts and its implications for mantle dynamics. *Gondwana Res.* 27(3), 1131–1152. doi:10.1016/j.gr.2014.09.003.
- Iwamori, H., Yoshida, M., Nakamura, H., 2022. Large-scale structures in the Earth’s interior: top-down hemispherical dynamics constrained by geochemical and geophysical approaches. *Front. Earth Sci.* 10, 1033378. doi:10.3389/feart.2022.1033378.

- Jeanloz, R., Morris, S., 1987. Is the mantle geotherm subadiabatic? *Geophys. Res. Lett.* 14(4), 335–338. doi:[10.1029/GL014i004p00335](https://doi.org/10.1029/GL014i004p00335).
- Johnson, D., Narayanan, R., 1997. Geometric effects on convective coupling and interfacial structures in bilayer convection. *Phys. Rev. E* 56(5), 5462–5472. doi:[10.1103/PhysRevE.56.5462](https://doi.org/10.1103/PhysRevE.56.5462).
- Kono, M., Roberts, P.H., 2002. Recent geodynamo simulations and observations of the geomagnetic field. *Rev. Geophys.* 40(4), 4-1–4-53. doi:[10.1029/2000RG000102](https://doi.org/10.1029/2000RG000102).
- Koper, K.D., Pyle, M.L., Franks, J.M., 2003. Constraints on aspherical core structure from *PKiKP-PcP* differential travel times. *J. Geophys. Res.* 108(B3), 2168. doi:[10.1029/2002JB001995](https://doi.org/10.1029/2002JB001995).
- Lambeck, K., Purcell, A., Zhao, S., 2017. The North American Late Wisconsin ice sheet and mantle viscosity from glacial rebound analyses. *Quat. Sci. Rev.* 158, 172–210. doi:[10.1016/j.quascirev.2016.11.033](https://doi.org/10.1016/j.quascirev.2016.11.033).
- Lau, H.C.P., Mitrovica, J.X., Auermann, J., Crawford, O., Al-Attar, D., Latychev, K., 2016. Inferences of mantle viscosity based on ice age data sets: radial structure. *J. Geophys. Res.: Solid Earth* 121(10), 6991–7012. doi:[10.1002/2016JB013043](https://doi.org/10.1002/2016JB013043).
- Lu, C., Grand, S.P., Lai, H., Garnero, E.J., 2019. TX2019slab: a new P and S tomography model incorporating subducting slabs. *J. Geophys. Res. Solid Earth* 124(11), 11549–11567. doi:[10.1029/2019jb017448](https://doi.org/10.1029/2019jb017448).
- McKenzie, D.P., Parker, R.L., 1967. The North Pacific: an example of tectonics on a sphere. *Nature* 216, 1276–1280. doi:[10.1038/2161276a0](https://doi.org/10.1038/2161276a0).
- Moore, D.R., Weiss, N.O., 1973. Two-dimensional Rayleigh-Bénard convection. *J. Fluid Mech.* 58(2), 289–312. doi:[10.1017/S0022112073002600](https://doi.org/10.1017/S0022112073002600).
- Morelli, A., Dziewonski, A.M., 1987. Topography of the core–mantle boundary and lateral homogeneity of the liquid core. *Nature* 325, 678–683. doi:[10.1038/325678a0](https://doi.org/10.1038/325678a0).
- Prakash, A., Yasuda, K., Otsubo, F., Kuwahara, K., Doi, T., 1997. Flow coupling mechanisms in two-layer Rayleigh–Bénard convection. *Exp. Fluid* 23(3), 252–261. doi:[10.1007/s003480050108](https://doi.org/10.1007/s003480050108).
- Ritsema, J., Deuss, A., van Heijst, H.J., Woodhouse, J.H., 2011. S40RTS: a degree-40 shear-velocity model for the mantle from new Rayleigh wave dispersion, teleseismic traveltime and normal-mode splitting function measurements. *Geophys. J. Int.* 184(3), 1223–1236. doi:[10.1111/j.1365-246X.2010.04884.x](https://doi.org/10.1111/j.1365-246X.2010.04884.x).
- Schubert, G., Turcotte, D.L., Olson, P., 2001. *Mantle Convection in the Earth and Planets*. Cambridge Univ. Press, London, p. 956. doi:[10.1017/CB09780511612879](https://doi.org/10.1017/CB09780511612879).
- Sun, Y., Xie, Y.-C., Xie, J.-X., Zhong, J.-Q., Zhang, J., Xia, K.-Q., 2024. Model for the dynamics of the large-scale circulations in two-layer turbulent convection. *Phys. Rev. Fluids* 9(3), 033501. doi:[10.1103/PhysRevFluids.9.033501](https://doi.org/10.1103/PhysRevFluids.9.033501).
- Sze, E.K.M., van der Hilst, R.D., 2003. Core mantle boundary topography from short period *PcP*, *PKP*, and *PKKP* data. *Phys. Earth Planet. Int.* 135(1), 27–46. doi:[10.1016/S0031-9201\(02\)00204-2](https://doi.org/10.1016/S0031-9201(02)00204-2).
- Tanaka, S., 2010. Constraints on the core-mantle boundary topography from *P4KP-PcP* differential travel times. *J. Geophys. Res.: Solid Earth* 115(B4), B04310. doi:[10.1029/2009JB006563](https://doi.org/10.1029/2009JB006563).
- Ukaji, K., Sawada, R., 1970a. Cellular convection in the two-layer fluid. *Abstracts of Meteorolog. Soc. Jpn. Meet.* 17, 96. (in Japanese).
- Ukaji, K., Sawada, R., 1970b. Cellular convection in the two-layer fluid (2). *Abstracts of Meteorolog. Soc. Jpn. Meet.* 18, 37 (in Japanese).
- Ukaji, K., Sawada, R., 1971. Cellular convection in the two-layer fluid (Theory 3). *Abstracts of Meteorolog. Soc. Jpn. Meet.* 20, 2 (in Japanese).
- Vecsey, L., 2003. *Chaos in Thermal Convection and the Wavelet Analysis of Geophysical Fields*. PhD thesis. Faculty of Mathematics and Physics, Charles University in Prague, p. 116.
- Vecsey, L., Yuen, D.A., Sevre, E.O.D., Dubuffet, F., 2003. Ultra-high Ra convection and applications of wavelet, in: *Abstracts of 8th International Workshop on Numerical Modeling of Mantle Convection and Lithospheric Dynamics*, Hrubá Skála, Czech Republic, p. 34.
- Versteeg, H.K., Malalasekera, W., 2007. *An Introduction to Computational Fluid Dynamics: The Finite Volume Method*. 2nd ed., Prentice Hall, U.K., p. 503.
- Wessel, P., Luis, J., Uieda, L., Scharroo, R., Wobbe, F., Smith, W.H.F., Tian, D., 2019. *The Generic Mapping Tools Version 6*. *Geochem. Geophys. Geosyst.* 20(11), 5556–5564. doi:[10.1029/2019GC008515](https://doi.org/10.1029/2019GC008515).
- Xie, Y.-C., Xia, K.-Q., 2013. Dynamics and flow coupling in two-layer turbulent thermal convection. *J. Fluid Mech.* 728, R1. doi:[10.1017/jfm.2013.313](https://doi.org/10.1017/jfm.2013.313).
- Yoshida, M., 2008a. Core-mantle boundary topography estimated from numerical simulations of instantaneous mantle flow. *Geochem. Geophys. Geosyst.* 9(7), Q07002. doi:[10.1029/2008GC002008](https://doi.org/10.1029/2008GC002008).
- Yoshida, M., 2008b. Mantle convection with longest-wavelength thermal heterogeneity in a 3-D spherical model: degree one or two? *Geophys. Res. Lett.* 35, L23302. doi:[10.1029/2008GL036059](https://doi.org/10.1029/2008GL036059).
- Yoshida, M., 2010. Preliminary three-dimensional model of mantle convection with deformable, mobile continental lithosphere. *Earth Planet. Sci. Lett.* 295(1-2), 205–218. doi:[10.1016/j.epsl.2010.04.001](https://doi.org/10.1016/j.epsl.2010.04.001).
- Yoshida, M., 2017. On approximations of the basic equations of terrestrial mantle convection used in published literature. *Phys. Earth Planet. Int.* 268, 11–17. doi:[10.1016/j.pepi.2017.05.006](https://doi.org/10.1016/j.pepi.2017.05.006).
- Yoshida, M., 2023a. How mantle convection drives the supercontinent cycle: mechanism, driving force, and substantivity, in: Duarte, J. (Ed.), *Dynamics of Plate Tectonics and Mantle Convection*. Elsevier, Amsterdam, Netherlands, p. 197–221. doi:[10.1016/B978-0-323-85733-8.00002-0](https://doi.org/10.1016/B978-0-323-85733-8.00002-0).
- Yoshida, M., 2023b. Stress state of the stable part of the Pacific Plate predicted by a numerical model of global mantle flow coupled with plate motion. *Lithosphere* 2023, 6563534. doi:[10.2113/2023/6563534](https://doi.org/10.2113/2023/6563534).
- Yoshida, M., Hamano, Y., 2016. Numerical studies on the dynamics of two-layer Rayleigh-Bénard convection with an infinite Prandtl number and large viscosity contrasts. *Phys. Fluids* 28(11), 116601. doi:[10.1063/1.4966685](https://doi.org/10.1063/1.4966685).
- Yoshida, M., Iwamori, H., Hamano, Y., Suetsugu, D., 2017. Heat transport and coupling modes in Rayleigh-Bénard convection occurring between two layers with largely different viscosities. *Phys. Fluids* 29(9), 096602. doi:[10.1063/1.4989592](https://doi.org/10.1063/1.4989592).
- Zhao, D., 2015. *Multiscale Seismic Tomography*. Springer Japan, Tokyo, p. 304. doi:[10.1007/978-4-431-55360-1](https://doi.org/10.1007/978-4-431-55360-1).